JFM RAPIDS
journals.cambridge.org/rapids

Impact of domain anisotropy on the inverse cascade in geostrophic turbulent convection

Keith Julien[1,†], **Edgar Knobloch**[2] **and Meredith Plumley**[1]

[1]Department of Applied Mathematics, University of Colorado, Boulder, CO 80309, USA

[2]Department of Physics, University of California, Berkeley, CA 94720, USA

The effect of domain anisotropy on the inverse cascade occurring within the geostrophic turbulence regime of rapidly rotating Rayleigh–Bénard convection is investigated. In periodic domains with square cross-section in the horizontal, a domain-filling dipole state is present. For rectangular periodic domains, a Kolmogorov-like flow parallel to the short side and consisting of a periodic array of alternating unidirectional jets with embedded vortices is observed, together with an underlying weak meandering transverse jet. Similar transitions occurring in weakly dissipative two-dimensional flows driven by externally imposed small-amplitude noise and in classical hydrostatic geostrophic turbulence are a consequence of inviscid conservation of energy and potential enstrophy, and can be understood using statistical mechanics considerations. Rotating Rayleigh–Bénard convection represents an important three-dimensional system with only one inviscid invariant which nonetheless exhibits large-scale structures driven by intrinsically generated fluctuations.

Key words: Bénard convection, geostrophic turbulence, quasi-geostrophic flows

1. Introduction

The quintessential paradigm for investigating the fundamentals of rotating thermally forced flows is provided by rotating Rayleigh–Bénard convection (RRBC) in a horizontal layer rotating about a vertical axis with constant angular velocity Ω, i.e. convection in a layer of Boussinesq fluid confined between flat horizontal rigidly rotating upper and lower boundaries maintaining a destabilizing temperature jump $\Delta T > 0$. Of particular relevance to the dynamics of stellar and planetary interiors, planetary atmospheres and terrestrial oceans is the regime of geostrophic turbulence where fluid motions are sufficiently constrained by rotation to enforce pointwise balance between the pressure gradient and the Coriolis force, otherwise known as

† Email address for correspondence: julien@colorado.edu

geostrophic balance. This balance is characteristic of rapidly rotating systems for which the convective Rossby number is small,

$$Ro \equiv \frac{\sqrt{g\alpha \Delta T/H}}{2\Omega} = \sqrt{\frac{Ra}{Pr}} E \ll 1. \tag{1.1}$$

This number denotes the ratio of the rotation time scale to the free-fall or free-rise time scale for a parcel of fluid with temperature difference ΔT relative to the ambient fluid. Here, g denotes the acceleration due to gravity, α is the thermal expansion coefficient and H is the layer depth. The second equality rewrites this definition in terms of quantities familiar from studies of Rayleigh–Bénard convection: the Rayleigh number Ra, the Ekman number E and the Prandtl number Pr, given by

$$Ra = \frac{g\alpha \Delta TH^3}{\nu\kappa}, \quad E = \frac{\nu}{2\Omega H^2}, \quad Pr = \frac{\nu}{\kappa}. \tag{1.2a–c}$$

These measure respectively the strength of the thermal forcing, the importance of viscous diffusion relative to rotation and the thermometric properties of the fluid through its kinematic viscosity ν and thermal diffusivity κ. Since Ra must be large to generate turbulence, the presence of geostrophic turbulence requires that E be correspondingly small. This regime can be accessed by exploring the simultaneous limits $Ra \to \infty$, $E \to 0$ such that $Ro \ll 1$. Unfortunately, this regime is inaccessible to both direct numerical simulations (DNS) of the Navier–Stokes equations (NSEs) and laboratory investigations. To date, the lowest achievable Ekman numbers are in the neighbourhood of $E = O(10^{-7})$, whereas an adequate exploration of geostrophic turbulence requires Ekman numbers that are much lower.

An alternative and fruitful approach that has recently been advanced (Julien & Knobloch 2007) employs an asymptotic reformulation of the NSEs for incompressible thermal convection valid in the limit $Ro \downarrow 0$ to derive a reduced system of partial differential equations (PDEs) called the non-hydrostatic quasi-geostrophic equations (NH-QGEs). This reduced system filters out fast inertial waves and thin Ekman boundary layers, and is therefore amenable to extensive numerical explorations. These have been validated qualitatively by DNS studies at moderately low Ro and E (Favier, Silvers & Proctor 2014; Guervilly, Hughes & Jones 2014; Stellmach *et al.* 2014; Plumley *et al.* 2016), and have enabled a comprehensive mapping of the Ra–Pr space (Julien *et al.* 2012; Rubio *et al.* 2014). Figure 1 illustrates volume renderings of the vorticity and streamfunction fields in the regime of geostrophic turbulence in a domain of unit aspect ratio in the horizontal. A remarkable feature of this state is the presence of a strong inverse energy cascade resulting in a box-scale condensate in the form of a vortex dipole. The feature appears to be barotropic (i.e. depth-independent), as demonstrated by, and most noticeable in, the barotropic vorticity and streamfunction fields (*b,c*). The barotropic dynamics satisfies the two-dimensional (2D) barotropic vorticity equation forced baroclinically by the underlying depth-dependent geostrophic turbulence and damped by viscosity (Rubio *et al.* 2014). The energetics of this process can be viewed as a two-way barotropic–baroclinic interaction: the barotropic dynamics is directly forced by and extracts energy from the convective (baroclinic) dynamics. This interaction can be highly efficient in that the barotropic vortex is capable of growing to large amplitudes with little impact on the underlying geostrophic turbulence, as measured by the small adjustment in convective (baroclinic) kinetic energy when the pathway to exciting the barotropic manifold is switched on at $t = 0$
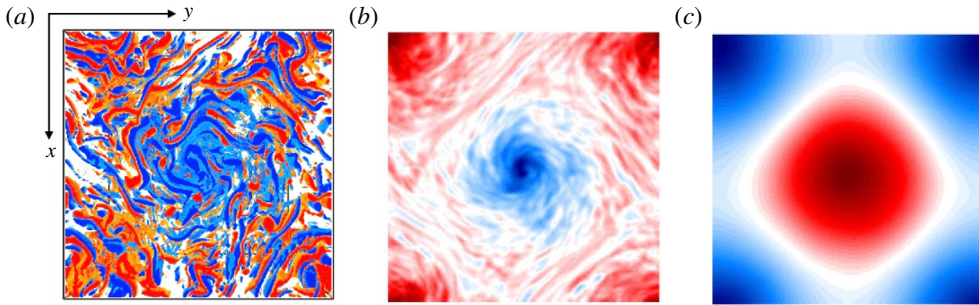
FIGURE 1. Volume render of geostrophic turbulence at $RaE^{4/3} = 90$, $Pr = 1$. Top view of (*a*) the total vertical vorticity ζ, (*b*) the barotropic vorticity $\langle\zeta\rangle$ and (*c*) the barotropic streamfunction $\langle\Psi\rangle$.

(Rubio *et al.* 2014). At the same time, the baroclinic fluctuations are aligned by the barotropic flow, leading to a self-sustaining process.

The generation of large-scale structure in turbulent flows is primarily investigated in 2D, and focuses on the 2D NSEs with damping (provided by Rayleigh friction) and dissipation (provided by viscosity), and driven by externally imposed noise, usually taken to be white (Smith & Yakhot 1994; Bouchet & Simonnet 2009; Frishman, Laurie & Falkovich 2017). Numerical study of this system in a periodic domain with a square aspect ratio also realizes condensation into a box-scale vortex structure. When the aspect ratio becomes elongated, turbulent jets oriented parallel to the short side form instead of a box-scale vortex. As shown recently (Frishman *et al.* 2017), these jets may be populated by large numbers of prominent vortices embedded in an anisotropic turbulent background state. This type of condensation process has also been examined using ideas from equilibrium statistical mechanics (Bouchet & Simonnet 2009; Bouchet & Venaille 2012), which predicts a transition from a box-scale vortex to a jet state as the aspect ratio increases and the domain becomes rectangular. Both the simulations and theory find that jets are already present when the elongation is of order 10 %. However, the statistical approach describes only box-scale structures and so cannot examine the finer details of the turbulent jets it predicts. In addition, the 2D system is a driven dissipative system, and any predictions from equilibrium statistical mechanics have to be treated with caution despite the similarities between the predictions and the numerical simulations.

In the present paper, we also identify a transition between a box-scale vortex dipole and jets, and find that jets first appear when the elongation is of order 10 %. However, our system is quite different from the 2D damped noise-driven NSEs studied by Smith & Yakhot (1994), Bouchet & Simonnet (2009) and Frishman *et al.* (2017) in that our equations are fully three-dimensional (3D) and the fluctuations driving the condensation process have to be determined self-consistently with the vortices or jets they produce. Thus, the noise process is both anisotropic and non-white, and the physics behind the condensation process necessarily differs. Our conclusion, elaborated further below, is that the condensation process is highly robust, with respect to both the physics behind the fluctuations and the substantially different nature of the governing equations themselves.

2. The non-hydrostatic reduced equations

A complete derivation and discussion of the NH-QGEs is presented in Sprague *et al.*
(2006), Julien & Knobloch (2007) and Julien *et al.* (2012). The equations are obtained
as the leading-order reduction of the incompressible NSEs based on a multiscale
asymptotic expansion in $Ro = E^{1/3} \equiv \epsilon \ll 1$ employing a small scale $L = \epsilon H \ll 1$
as well as the large vertical scale H. For the case of stress-free upper and lower
boundaries, the leading-order velocity field $\boldsymbol{u} \equiv (\boldsymbol{u}_\perp, W)$ is in geostrophic balance,
i.e. $\widehat{\boldsymbol{z}} \times \boldsymbol{u}_\perp = -\nabla_\perp p$. It follows that the horizontal velocity field is non-divergent,
with $\boldsymbol{u}_\perp \equiv (u, v, 0) = (-\partial_y \Psi, \partial_x \Psi, 0)$, where the pressure $p \equiv \Psi$ is the geostrophic
streamfunction. The reduced NH-QGEs governing the motion of the fluid are

$$D_t^\perp \zeta - \partial_Z W = \nabla_\perp^2 \zeta, \tag{2.1}$$

$$D_t^\perp W + \partial_Z \Psi = \frac{\widetilde{Ra}}{Pr} \Theta' + \nabla_\perp^2 W, \tag{2.2}$$

$$D_t^\perp \Theta' + W \partial_Z \overline{\Theta} = \frac{1}{Pr} \nabla_\perp^2 \Theta', \tag{2.3}$$

$$\partial_\tau \overline{\Theta} + \partial_Z (\overline{W\Theta'}) = \frac{1}{Pr} \partial_{ZZ} \overline{\Theta}, \tag{2.4}$$

capturing respectively the evolution of vertical vorticity $\zeta = -\nabla_\perp^2 \Psi$, vertical velocity
W and temperature $\Theta = \overline{\Theta} + \epsilon \Theta'$ at the reduced Rayleigh number $\widetilde{Ra} = Ra\epsilon^4$ for a
given Prandtl number Pr. The temperature is decomposed into a mean (horizontally
averaged) component $\overline{\Theta}$ evolving on the slow time scale $\tau = \epsilon^2 t$ and a small
fluctuating component Θ'. Here, $D_t^\perp \equiv \partial_t + \boldsymbol{u}_\perp \cdot \nabla_\perp$ denotes the horizontal material
derivative. The system is solved with impenetrable stress-free fixed-temperature
boundary conditions,

$$\overline{\Theta} = 1, \; W = \Theta' = 0 \text{ at } Z = 0, \quad \text{and} \quad \overline{\Theta} = 0, \; W = \Theta' = 0 \text{ at } Z = 1. \tag{2.5a,b}$$

The NH-QGEs are discretized in the horizontal and vertical spatial directions using
a sparse Fourier–Chebyshev spectral decomposition (Julien & Watson 2009). They are
then time evolved using a third-order semi-implicit explicit Runge–Kutta scheme.

3. Results and discussion

In the following, we present results for RRBC obtained from a series of simulations
of the NH-QGE system (2.1)–(2.5) performed within the geostrophic turbulence
regime at $\widetilde{Ra} = 90$, $Pr = 1$. The horizontal aspect ratio $1 : \Gamma$ is varied from $1 : 1$ to
$1 : 6$. All cases exhibit similar efficiency in heat transport as measured by the Nusselt
number, namely $Nu = 36.84 \pm 1.97$.

3.1. *Visualizations*

Figure 2 depicts the top views of volume renderings of the total vertical vorticity ζ (*a*),
the barotropic vorticity $\langle \zeta \rangle$ (*b*) and the barotropic streamfunction $\langle \Psi \rangle$ (*c*). Here, $\langle \cdots \rangle$
indicates an average in the vertical. The barotropic vortex dipole present at aspect
ratio $1 : 1$ (top row) is replaced by a state of approximately parallel (i.e. banded)
flow consisting of an alternating sequence of cyclonic and anticyclonic vortical bands.
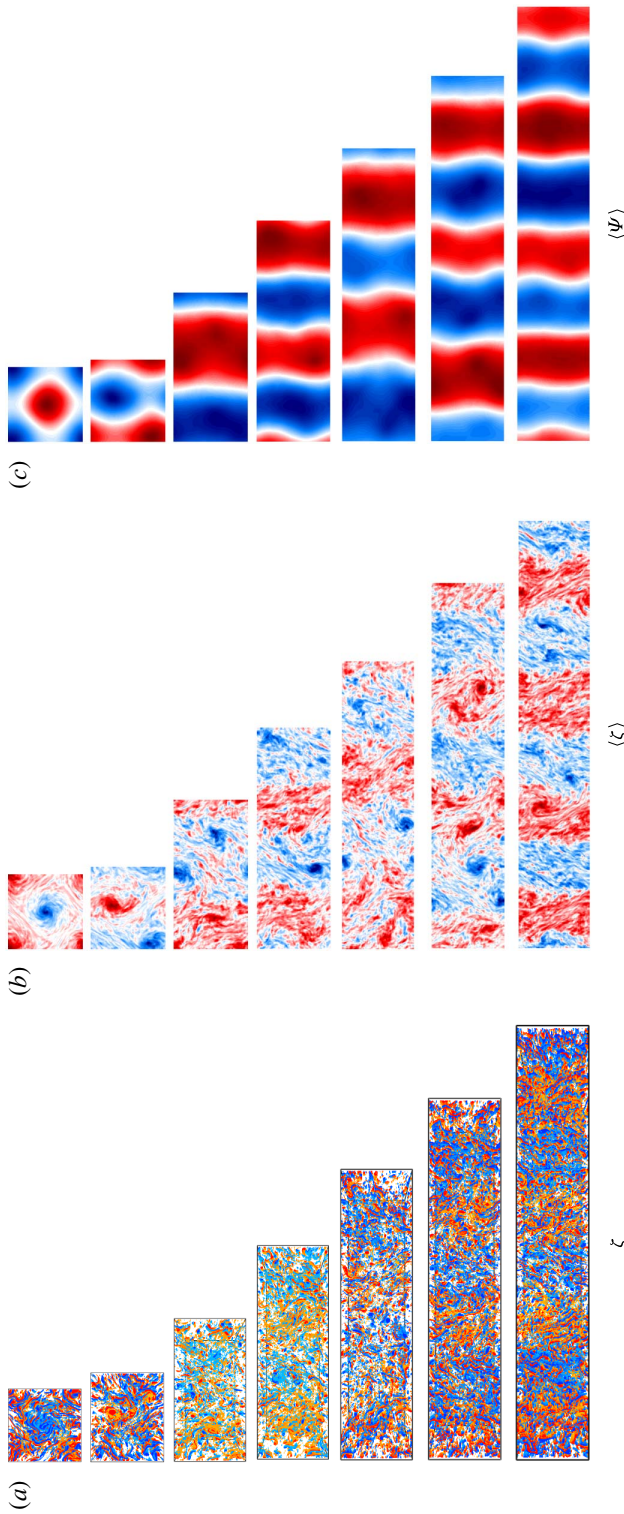This transition first occurs at an aspect ratio of approximately $1 : 1.1$ (second row)

FIGURE 2. Top view of a suite of simulations using the NH-QGEs for RRBC with impenetrable stress-free fixed-temperature boundaries. All simulations were performed at $\widetilde{Ra} = 90$, $Pr = 1$. (a) The total vorticity ζ, (b) the barotropic vorticity $\langle\zeta\rangle$ and (c) the barotropic streamfunction $\langle\Psi\rangle$. In units of a fixed x-horizontal box scale $L_x = 10L_c$ (where $L_c = 4.82E^{1/3}H$ is the critical wavelength for convection), the domain aspect ratio $(1 : \Gamma)L_x$ increases from $1:1$ (upper row) to $1:1.1$ (second row) and incrementally from $1:2$ to $1:6$ (remaining rows). It should be noted that x is in the vertical direction with y plotted horizontally. Banded flow of alternating cyclonicity when $\Gamma = 2$, and a doubling, tripling and quadrupling of the band structure at $\Gamma = 3$, 5 and 6 respectively is evident. The second row $(\Gamma = 1.1)$ shows that the transition to banded flow occurs upon even a small departure from isotropy. The resolution in the x, y, Z directions is $144 \times 144\Gamma \times 192$.

and is most prominently revealed in the rendering of the barotropic streamfunction; $\langle \zeta \rangle$ exhibits greater spatial complexity due to higher spatial derivatives. We see that strong vortical eddies persist within a band of given cyclonicity and that small-scale geostrophic turbulence is globally advected and organized by the banded large-scale flow. The latter resembles the small-scale filamentary structures in figure 1(*a*). From a more global perspective, the aspect ratio Γ provides a selection mechanism for the number of alternating bands or jets. It can be seen that an increase from $\Gamma = 2$ to $\Gamma = 3$ results in a doubling of the number of alternating bands from one to two. The latter persists for $\Gamma = 4$ before losing stability to a state of three alternating bands at an aspect ratio of $\Gamma = 5$ and then four at $\Gamma = 6$.

Inspection of the horizontal velocity fields offers another viewpoint for interpreting the large-scale barotropic structure (figure 3). In the following, we refer to the velocity components $u = -\partial_y \Psi$ and $v = \partial_x \Psi$ as parallel and transverse respectively. The parallel velocity field (*a,c,e,g*) clearly shows a state resembling Kolmogorov flow, i.e. alternating bands of unidirectional but oppositely directed turbulent flow (*a,e*). Averaging along the x direction reveals a jet structure that is sawtooth in shape in the y or transverse direction (dashed lines, *c,g*), with small root mean square (RMS) fluctuations (solid lines, *c,g*). This unidirectional jet structure is found at all sufficiently non-square aspect ratios (figure 2). Observations of v (*b,d,f,h*) indicate coexistence with a weak meandering transverse jet (*b,f*). Averaging in the y direction (dashed lines, *d,h*) shows that the transverse mean flow is substantially weaker than the parallel flow (by a factor of approximately 10). The RMS fluctuations about this profile are large, indicating that the transverse mean flow is highly oscillatory (solid lines, *d,h*). Figure 3(*i,j*) illustrates the persistence of the parallel and transverse flows with time through Hovmöller diagrams. Here, we see that after an initial transient, stable parallel jets are formed while the antisymmetric transverse flow exhibits random switching.

3.2. *Energetics*

In the absence of dissipation, and like the incompressible NSEs, all QG systems conserve the volume-averaged energy $\mathcal{E}$ and the pointwise potential vorticity $\mathcal{PV}$. For the NH-QGEs (2.1)–(2.4), these are given by

$$\mathcal{E} = \left\langle \left(\frac{1}{2}\overline{|\nabla_\perp \Psi|^2 + W^2} \right) + \frac{\widetilde{Ra}}{Pr} \left(\overline{\Theta'^2} + \epsilon^{-2} \left(\overline{\Theta} - z \right)^2 \right) \right\rangle, \qquad (3.1)$$

$$\mathcal{PV} = \zeta - J\left[W, \frac{\Theta'}{\partial_z \overline{\Theta}} \right] + \partial_z \left(\frac{\Theta'}{\partial_z \overline{\Theta}} \right), \qquad (3.2)$$

where $J[f, g] = \partial_x f \partial_y g - \partial_y f \partial_x g$. As a consequence of strong vertical motion, with $|W| \sim |\boldsymbol{u}_\perp|$, $\mathcal{E}$ and $\mathcal{PV}$ are not solely functionals of the geostrophic streamfunction Ψ: the second and third terms in (3.2) represent ageostrophic baroclinic contributions to $\mathcal{PV}$. Sole functional dependence on Ψ may be recovered from the NH-QGE system only in the limit of strong stratification where $\partial_z \overline{\Theta} \to \epsilon^{-1}$, $\partial_z \to \epsilon^{-1}$ and $W \to \epsilon$. Here, hydrostatic balance in (2.2) implies $\Theta' \to (Pr/\widetilde{Ra})\partial_z \Psi$ and the classical hydrostatic quasi-geostrophic equation is recovered. In this case, the volume-averaged potential enstrophy $\langle \overline{\mathcal{PV}^2} \rangle$ becomes the second conserved quantity required to guarantee a dual cascade.
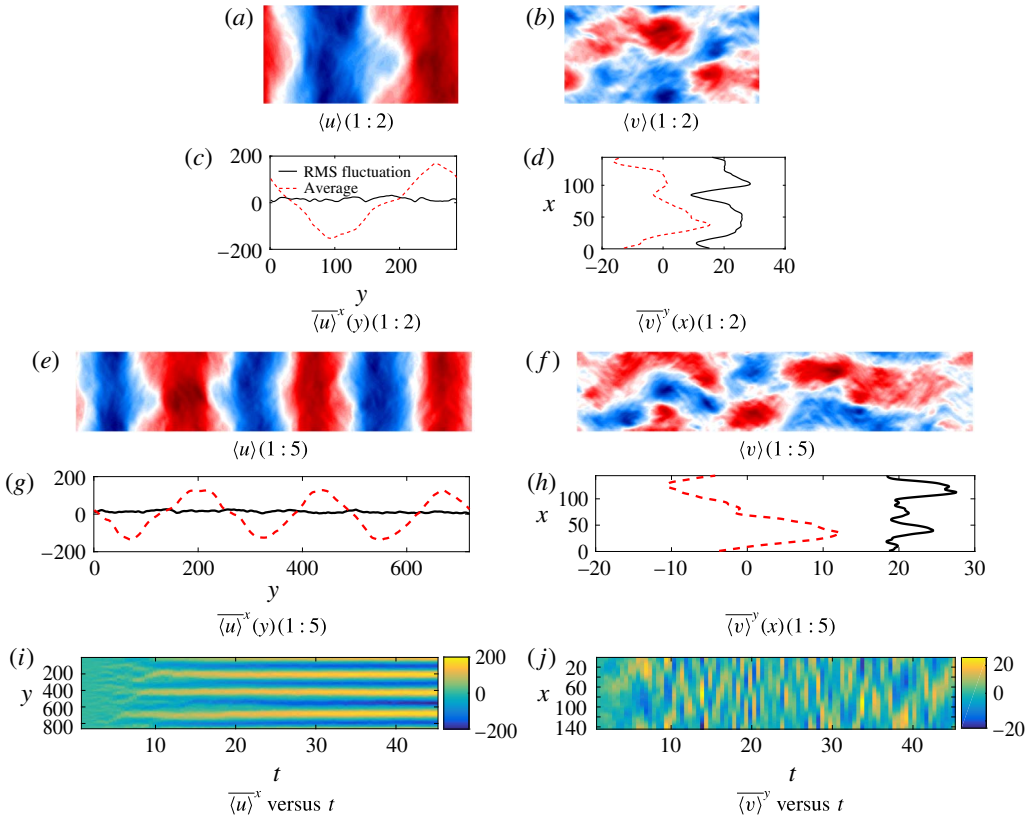
FIGURE 3. (*a–h*) Parallel and transverse barotropic velocity fields $\langle u \rangle$ (*a,c,e,g*) and $\langle v \rangle$ (*b,d,f,h*). Aspect ratios of $1:2$ and $1:5$ are depicted in (*a,b,c,d*) and (*e,f,g,h*) respectively. Here, $\overline{f}^d$ indicates averaging of f in the d direction. The average and RMS fluctuations of $\langle u \rangle$ in the parallel direction, i.e. averaging in the x direction, reveal a Kolmogorov-like velocity profile, and the fluctuations of $\langle v \rangle$ in the transverse direction reveal the presence of a meandering jet (red dashed lines). The amplitude of the RMS fluctuations about these profiles is shown by solid black lines. (*i,j*) Hovmöller diagrams of (*i*) $\overline{\langle u \rangle}^x$ and (*j*) $\overline{\langle v \rangle}^y$ for an aspect ratio of $1:5$ at time intervals $\Delta t = 0.5$.

As already noted, however, the dynamics within the barotropic subspace provides an alternative pathway for an inverse cascade. Depth-averaging of the vertical vorticity equation (2.1) gives the barotropic vorticity equation (BVE),

$$\partial_t \langle \zeta \rangle + J[\langle \Psi \rangle, \langle \zeta \rangle] = -\langle J[\Psi', \zeta'] \rangle + \nabla_\perp^2 \langle \zeta \rangle, \tag{3.3}$$

indicating that the material growth of $\langle \zeta \rangle$ depends on the net balance between the two terms on the right-hand side, i.e. between the baroclinic forcing and the barotropic viscous dissipation. In the absence of forcing and damping, the conserved quantities are the volume-averaged barotropic energy and enstrophy,

$$\mathcal{E}_{bt} = \tfrac{1}{2}\langle \overline{|\nabla_\perp \langle \Psi \rangle|^2} \rangle, \quad \mathcal{Z}_{bt} = \overline{\langle \zeta \rangle^2} = \langle \overline{(\nabla_\perp^2 \langle \Psi \rangle)^2} \rangle. \tag{3.4a,b}$$

Both are sole functionals of $\langle \Psi \rangle$, suggesting a dual cascade. For all aspect ratios, we find that the evolution of the volume-averaged kinetic energy is similar to the
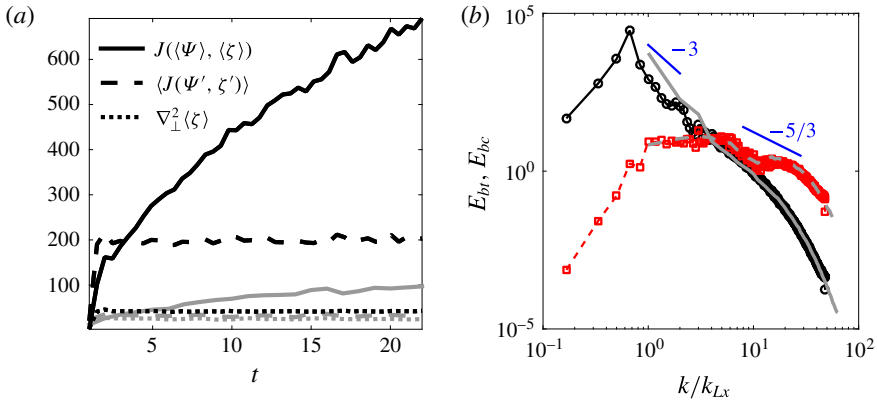
FIGURE 4. (*a*) Term by term decomposition of the barotropic vorticity equation (3.3) showing unbounded growth in the barotropic mode for $\Gamma = 6$ (black) and $\Gamma = 1$ (grey). (*b*) One-dimensional barotropic (solid) and baroclinic (dashed) kinetic energy spectra as a function of k/k_{Lx} for $\Gamma = 6$, with the corresponding results for $\Gamma = 1$ in grey. Here, $k_{Lx} = 2\pi/L_x$ denotes the box wavenumber in the x direction. Peak energy scales $k/k_{Lx} = 4/6$ for $\Gamma = 6$ and $k/k_{Lx} = 1$ for $\Gamma = 1$ characterize the jet scale.

isotropic case. Figure 4(*a*) illustrates the decomposition of the right-hand side of the BVE (3.3) as a function of time for $\Gamma = 1$ and $\Gamma = 6$. The figure clearly demonstrates that in both cases the convective forcing $\langle J[\Psi', \zeta'] \rangle$ and damping $\nabla_\perp^2 \langle \zeta \rangle$ are saturated but unbalanced, resulting in unbounded growth of the large-scale barotropic mode. However, despite this similarity, notable distinctions exist in the energetics. Figure 4(*b*) shows the corresponding kinetic energy spectra as a function of the renormalized horizontal wavenumber k/k_{Lx}, where $k = \sqrt{k_x^2 + k_y^2}$ and $k_{Lx} = 2\pi/L_x$ are associated with the box dimension L_x. Here,

$$E(k) = \int_0^{2\pi} E(\boldsymbol{k})k \, \mathrm{d}\phi_k, \qquad (3.5)$$

where in polar representation $k = |\boldsymbol{k}|$ and $\tan \phi_k = k_y/k_x$. The spectra have also been decomposed into barotropic (bt) and baroclinic (bc) components. For both $\Gamma = 1$ and $\Gamma = 6$ (and indeed all intermediate cases), the barotropic signature (solid curves) exhibits a steep power law with $E_{bt}(k) \sim k^{-3}$, while the baroclinic signature (dashed curves) gains dominance at higher wavenumber and exhibits a shallower instantaneous power $E_{bc}(k) \sim k^{-5/3}$ (Rubio *et al.* 2014). The total kinetic energy spectrum $E_{bt} + E_{bc}$ exhibits a steep to shallow transition in the power law exponents, a result reminiscent of the Nastrom–Gage spectrum observed in atmospheric and oceanic measurements (Nastrom & Gage 1985). In the present RRBC case, however, the k^{-3} barotropic spectrum is a consequence of the large-scale condensate (Smith & Waleffe 1999). For $\Gamma = 1$ (grey curve), we observe that the most energetic barotropic scale is $k/k_{Lx} = 1$, indicating that the large-scale condensate (the vortex dipole) has reached the box scale, the largest scale possible. For anisotropic aspect ratios, the most energetic scale is that associated with the unidirectional jet occurring at a scale intermediate to the box dimensions, i.e. $k_{Ly} < k < k_{Lx}$. For $\Gamma = 6$, where four jets are observed, this occurs at $k/k_{Lx} = 4/6$ (see the solid line in figure 4*b*), with a steep decline in power

from its peak to the largest box scale $2\pi/k_{Ly}$. These larger scales are associated with the weaker meandering transverse jet (see figure 3b,f). For $2 \leqslant \Gamma \leqslant 6$, we observe maximal power in the barotropic energy spectra at $1/2 \leqslant k/k_{Lx} \leqslant 4/6$, or, equivalently, $3/2 \leqslant L/L_x \leqslant 2$.

The flow of energy associated with the generation of large-scale dynamics in the barotropic subspace can be determined from the nonlinear advection term in (3.3). Accordingly, we detail how power is transferred to the horizontal wavenumber $\boldsymbol{k}$ through triadic interactions involving wavenumbers $\boldsymbol{p}$ and $\boldsymbol{q}$ such that $\boldsymbol{p} + \boldsymbol{q} + \boldsymbol{k} = \boldsymbol{0}$. We define the transfer functions

$$T_{kpq} = b_{pq} \mathrm{Re}[\langle \hat{\Psi}_k \rangle \langle \hat{\Psi}_p \rangle \langle \hat{\Psi}_q \rangle] \delta_{p+q+k,0}, \tag{3.6}$$

$$b_{pq} = b_{qp} = \tfrac{1}{2}(p^2 - q^2)(p_x q_y - p_y q_x), \tag{3.7}$$

where Re denotes the real part and $\delta_{p+q+k,0}$ is the Kronecker delta function. Anisotropy is handled by replicating a $1 : \Gamma$ barotropic field Γ times to form a periodic square of size $(\Gamma L_x)^2$. Owing to this periodic extension, the power map of a 2D Fourier transform of the barotropic field contains the non-integer wavenumber array $(k_x, k_y) = (2\pi/L_x)(i/\Gamma, j/\Gamma)$, with $i, j = 0, 1, \ldots, N_x \Gamma$. The array is sparse due to zero row entries corresponding to wavenumbers k_x with non-integer values i/Γ that do not fulfil the periodicity of the $(0, L_x)$ domain. To avoid the impact of these zero entries when averaging over annular or spherical shells in wavenumber space, we invoke coarse-graining by averaging over blocks of Γ^2 entries: the block associated with integer wavelengths $(2\pi/L_x)(p, q)$ is indexed by

$$i_x = p - \frac{i - 1}{\Gamma}, \quad i = 1, \Gamma; \quad i_y = q - \frac{j - 1}{\Gamma}, \quad j = 1, \Gamma. \tag{3.8a,b}$$

The result of coarse-graining is a power map array that contains integer wavenumbers $(k_x, k_y) = (2\pi/L_x)(p, q)$, with $p, q = 0, 1, \ldots, N_x$. The coarse-grained transfer map

$$T_{kp} = \int k \, \mathrm{d}\phi_k \int p \, \mathrm{d}\phi_p \sum_q T_{kpq} \tag{3.9}$$

details the transfer of energy from wavenumber p to k. Figure 5 illustrates three cases: $\Gamma = 1$ and the coarse-grained transfer maps for $\Gamma = 3$ and 6. The power signature in the super- and sub-off-diagonal lines in all barotropic self-interaction T_{kp} maps indicates the existence of a forward or direct cascade, i.e. direct transfer of spectral power from low to high k at constant wavenumber p. The non-local inverse cascade occurs for $p \gg k$ and corresponds to the direct transfer of power from the high p wavenumbers to $k \approx 1$. Likewise, when $p \ll k$, energy is extracted from high k wavenumbers and transferred to $p \approx 1$. It should be recalled that for $\Gamma > 1$, the wavenumber $(p, k) = (1, 1)$ associated with the large-scale structure is associated with subharmonic wavenumbers identified in (3.8) with $p, q = 1$.

3.3. *Potential vorticity*

From the full NH-QGE system, the barotropic and baroclinic potential vorticities are given by

$$\mathcal{PV}_{bt} = \langle \zeta \rangle - \left\langle J\left[W, \frac{\Theta'}{\partial_Z \overline{\Theta}}\right] \right\rangle, \quad \mathcal{PV}_{bc} = \zeta' - J\left[W, \frac{\Theta'}{\partial_Z \overline{\Theta}}\right]' + \partial_Z \left(\frac{\Theta'}{\partial_Z \overline{\Theta}}\right). \tag{3.10a,b}$$
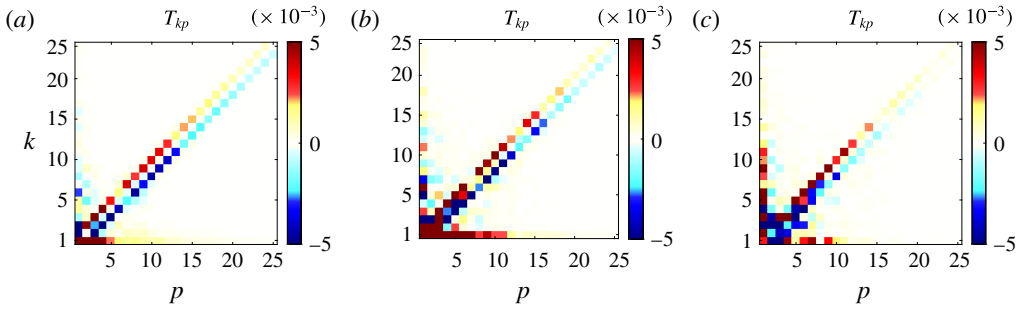
FIGURE 5. Spectral transfer maps of barotropic self-interaction for aspect ratios of $1:1$ (*a*), $1:3$ (*b*) and $1:6$ (*c*), showing how energy is transferred from wavenumbers p to wavenumbers k. The results in (*b,c*) have been coarse-grained to manage the non-integer wavenumbers arising from the anisotropy of the domain.
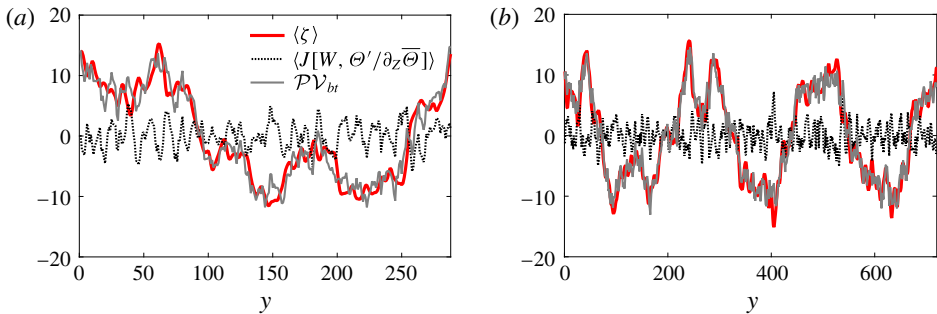

FIGURE 6. The barotropic potential vorticity $\mathcal{PV}_{bt}$ and its decomposition for aspect ratios of $1:2$ (*a*) and $1:5$ (*b*). The $\langle \zeta \rangle$ term dominates, suggesting the linear relation $\mathcal{PV}_{bt} \approx \langle \zeta \rangle$.

Details of the characteristics of these two quantities are illustrated in figure 6, with results for aspect ratios of $1:2$ and $1:5$. A snapshot of $\mathcal{PV}_{bt}$ as a function of y indicates that it is dominated by the barotropic vorticity $\langle \zeta \rangle$. This signal oscillates in y, reflecting the spontaneous generation of a Kolmogorov-like flow. Consistent with the inverse energy cascade, we find that the magnitude of this signal is unbounded in time. In contrast, the baroclinic contribution to $\mathcal{PV}_{bt}$ remains bounded and fluctuates randomly about zero without coherence. This result suggests that the barotropic dynamics is essentially linear. In contrast, $\mathcal{PV}_{bc}$ and its component terms, which are of roughly equal magnitude, vary rapidly about zero mean and saturate in time (not shown). The finding that the dissipation and the forcing are both weak suggests that the barotropic manifold is amenable to the application of equilibrium statistical mechanics (Bouchet & Venaille 2012).

4. Conclusion

In this paper, we have confirmed, following earlier work (Julien *et al.* 2012; Rubio *et al.* 2014), that geostrophic turbulence is unstable to the formation of large-scale vortices, and investigated the properties of this state when the doubly periodic domain we use in the horizontal changes from square to rectangular. We have shown that with increasing domain anisotropy, the large-scale vortex structure is replaced by a

shear flow of Kolmogorov type parallel to the shorter side and superposed on the turbulent state. The flow has jet-like structure with a well-defined characteristic scale comparable to the short box scale that forms spontaneously. It is neither externally imposed nor the result of imposed external stirring (Smith & Yakhot 1994; Bouchet & Simonnet 2009; Frishman *et al.* 2017) – here, the flow is maintained by 3D turbulent fluctuations that are determined self-consistently. The jets all have a well-defined mean separation that depends on the aspect ratio but undergo meander that may be intrinsic or driven by fluctuations. Evidently, jet formation does not require the presence of a β term.

These predictions resemble qualitatively the predictions from both numerical simulations of the damped 2D NSEs driven by imposed white noise (Smith & Yakhot 1994; Bouchet & Simonnet 2009; Frishman *et al.* 2017) and those from equilibrium statistical mechanics for 2D flows (Bouchet & Venaille 2012). Since the noise is imposed in the simulations, it cannot respond to the box-scale structures that evolve. This is also the case in the equilibrium statistical description, where noise must be assumed to be present to drive the system to equilibrium but the equilibrium reached is independent of the noise. The equilibrium statistical mechanics approach is based on maximizing the entropy, defined in terms of the vertical vorticity, subject to constraints derived from the inviscid equations of motion. The variational problem leads to a monotonically increasing relation between the most probable values of the vorticity $\bar{\zeta}$ and the streamfunction $\bar{\Psi}$. We assume that these values are those realized by the flow, and hence drop the overbars in the discussion that follows. Whether the predictions of this type of theory are relevant to a 3D forced dissipative flow such as geostrophic turbulence remains a question, however. Figure 7 provides evidence that a $\zeta(\Psi)$ relation in fact exists for both $\Gamma = 1$ and $\Gamma \neq 1$, and is qualitatively similar to that found in 2D hydrodynamics. Indeed, if we suppose, following Bouchet & Simonnet (2009) and Bouchet & Venaille (2012), a relation of the form $\zeta = a_2\Psi + a_4\Psi^3 + \cdots$, we conclude from figure 7(*a*) that in both cases $a_2 < 0$, $a_4 < 0$. The non-zero value of a_4 is important in determining the nature of the transition from the box-scale dipole present when $\Gamma = 1$ to the jet-like flow parallel to the shorter side present when $\Gamma \gtrsim 1$, a transition whose presence here accords with both simulations of the damped 2D NSEs driven by noise (Bouchet & Simonnet 2009; Frishman *et al.* 2017) and the prediction from equilibrium statistical mechanics (Bouchet & Simonnet 2009; Bouchet & Venaille 2012). The latter predicts the presence of a phase transition from the dipole state to a parallel shear flow already at small values of the elongation $\Gamma - 1$ (Bouchet & Simonnet 2009; Bouchet & Venaille 2012), a result qualitatively similar to both the 2D simulations and our self-consistent 3D simulations in figure 2 (second row: $\Gamma = 1.1$).

While the correspondence between our numerical results and equilibrium statistical mechanics theory is encouraging, it is also evident that our system is not an equilibrium system – it is a forced dissipative system. In this case, as already discussed, we expect to see an inverse energy cascade towards large scales and a direct entropy cascade to small scales. However, if both the forcing and the dissipation are appropriately weak on the large scales of interest, which we believe to be the case, the resulting non-equilibrium states that are observed are nevertheless expected to be close to the equilibrium states identified in the equilibrium statistical mechanics approach, a prediction corroborated in DNS of a stochastically driven vorticity equation in 2D (Smith & Yakhot 1994; Bouchet & Simonnet 2009; Frishman *et al.* 2017). In particular, the transition from a dipole flow to a parallel shear flow with increasing elongation, predicted by the statistical mechanics approach, persists into the non-equilibrium regime (see figure 23 of Bouchet & Venaille 2012).
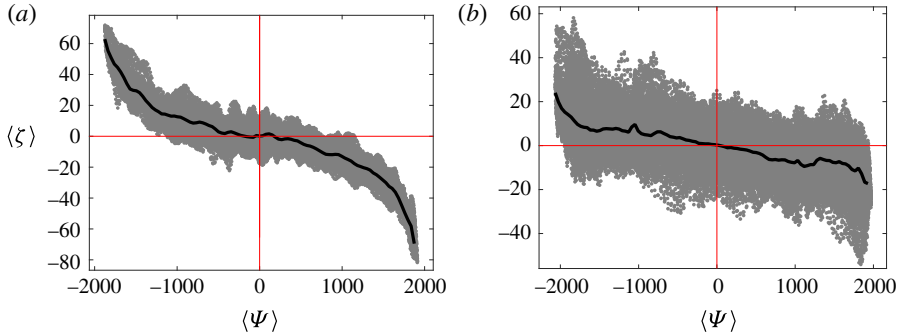
FIGURE 7. Scatter plots of $\langle \zeta \rangle$ versus $\langle \Psi \rangle$ for aspect ratios of $1:1$ (*a*) and $1:5$ (*b*), suggesting a functional relation (black curve) obtained by pointwise averaging. The plots indicate that $a_2 a_4 > 0$.

The above theory (Bouchet & Venaille 2012) has been developed for 2D flows. Our system is, in contrast, fully 3D, at least on small scales. However, the large-scale barotropic mode studied here obeys 2D dynamics driven by stochastic baroclinic forcing, and therefore shares many of the properties of these flows discussed by Bouchet & Venaille (2012) and Frishman *et al.* (2017). In particular, we expect that our flows should also undergo a transition with increasing anisotropy from a dipole flow to a parallel shear flow, a prediction confirmed in our simulations. We emphasize that these are performed on an asymptotically reduced model valid in the limit $Ro \rightarrow 0$ (Julien *et al.* 2012; Rubio *et al.* 2014). Given that the predictions of this model have been confirmed in subsequent simulations of the primitive equations at $E = 10^{-7}$ (Stellmach *et al.* 2014), $E = 10^{-6}$ (Favier *et al.* 2014) and $E = 5 \times 10^{-6}$ (Guervilly *et al.* 2014), we expect that our findings will also apply to the NSEs at sufficiently low Ekman numbers. That this is in fact the case is demonstrated by Guervilly & Hughes (2017), who show that when $E = 10^{-5}$, jets also appear when the elongation exceeds 10 %. The characteristic horizontal scales of the multi-jet states for larger elongations are also comparable. However, there are some differences too, in that Guervilly and Hughes also observe quite long-lived cyclonic vortices within their jets, whereas our system exhibits both cyclonic and anticyclonic vortices in equal numbers. This is a consequence of the reflection symmetries $x \rightarrow -x$, $y \rightarrow -y$ of the NH-QGE system that are present at leading order in the limit $Ro \rightarrow 0$ ($E \rightarrow 0$).

The above discussion indicates that the formation of large-scale structures, be they box-scale vortices or jets, is a very robust phenomenon, independent of the details of the fluctuations driving the system, independent of the specific system studied and even independent of its dimensionality, provided only that the flow is strongly anisotropic. Thus, large-scale vortices are also present in 3D non-rotating systems, provided that the fluid layer is sufficiently thin, thereby forcing the turbulent flow to be anisotropic on large scales (Xia *et al.* 2008; Xia, Shats & Falkovich 2009). We expect that in the presence of doubly periodic boundary conditions, this system will also undergo a transition with increasing domain anisotropy from the large-scale vortex state observed in square domains to a parallel shear flow, although this is of course difficult to confirm in experiments carried out in bounded domains. In thicker layers, the large-scale vortex reduces vertical motion, rendering the system susceptible to upscale energy cascade (Xia *et al.* 2011) and reinforcing the vortex. In this case, too, we expect a transition to large-scale shear flow with increased anisotropy much

as occurs in convectively driven turbulence (Goluskin *et al.* 2014). Both conjectures are amenable to confirmation by DNS.

Acknowledgements

References

BOUCHET, F. & SIMONNET, E. 2009 Random changes of flow topology in two-dimensional and geophysical turbulence. *Phys. Rev. Lett.* **102**, 094504.

BOUCHET, F. & VENAILLE, A. 2012 Statistical mechanics of two-dimensional and geophysical flows. *Phys. Rep.* **515**, 227–295.

FAVIER, B., SILVERS, L. J. & PROCTOR, M. R. E. 2014 Inverse cascade and symmetry breaking in rapidly rotating Boussinesq convection. *Phys. Fluids* **26**, 096605.

FRISHMAN, A., LAURIE, J. & FALKOVICH, G. 2017 Jets or vortices – what flows are generated by an inverse turbulent cascade? *Phys. Rev. Fluids* **2**, 032602(R).

GOLUSKIN, D., JOHNSTON, H., FLIERL, G. R. & SPIEGEL, E. A. 2014 Convectively driven shear and decreased heat flux. *J. Fluid Mech.* **759**, 360–385.

GUERVILLY, C. & HUGHES, D. W. 2017 Jets and large-scale vortices in rotating Rayleigh–Bénard convection. *Phys. Rev. Fluids* **2** (11), 113503.

GUERVILLY, C., HUGHES, D. W. & JONES, C. A. 2014 Large-scale vortices in rapidly rotating Rayleigh–Bénard convection. *J. Fluid Mech.* **758**, 407–435.

JULIEN, K. & KNOBLOCH, E. 2007 Reduced models for fluid flows with strong constraints. *J. Math. Phys.* **48**, 065405.

JULIEN, K., RUBIO, A. M., GROOMS, I. & KNOBLOCH, E. 2012 Statistical and physical balances in low Rossby number Rayleigh–Bénard convection. *Geophys. Astrophys. Fluid Dyn.* **106**, 392–428.

JULIEN, K. & WATSON, M. 2009 Efficient multi-dimensional solution of PDEs using Chebyshev spectral methods. *J. Comput. Phys.* **228**, 1480–1503.

NASTROM, G. D. & GAGE, K. S. 1985 A climatology of atmospheric wavenumber spectra of wind and temperature observed by commercial aircraft. *J. Atmos. Sci.* **42**, 950–960.

PLUMLEY, M., JULIEN, K., MARTI, P. & STELLMACH, S. 2016 The effects of Ekman pumping on quasi-geostrophic Rayleigh–Bénard convection. *J. Fluid Mech.* **803**, 51–71.

RUBIO, A. M., JULIEN, K., KNOBLOCH, E. & WEISS, J. B. 2014 Upscale energy transfer in three-dimensional rapidly rotating turbulent convection. *Phys. Rev. Lett.* **112**, 144501.

SMITH, L. M. & WALEFFE, F. 1999 Transfer of energy to two-dimensional large scales in forced, rotating three-dimensional turbulence. *Phys. Fluids* **11**, 1608–1622.

SMITH, L. M. & YAKHOT, V. 1994 Finite-size effects in forced two-dimensional turbulence. *J. Fluid Mech.* **274**, 115–138.

SPRAGUE, M., JULIEN, K., KNOBLOCH, E. & WERNE, J. 2006 Numerical simulation of an asymptotically reduced system for rotationally constrained convection. *J. Fluid Mech.* **551**, 141–174.

STELLMACH, S., LISCHPER, M., JULIEN, K., VASIL, G., CHENG, J. S., RIBEIRO, A., KING, E. M. & AURNOU, J. M. 2014 Approaching the asymptotic regime of rapidly rotating convection: boundary layers versus interior dynamics. *Phys. Rev. Lett.* **113**, 254501.

XIA, H., BYRNE, D., FALKOVICH, G. & SHATS, M. 2011 Upscale energy transfer in thick turbulent fluid layers. *Nat. Phys.* **7**, 321–324.

XIA, H., PUNZMANN, H., FALKOVICH, G. & SHATS, M. 2008 Turbulence condensate interaction in two dimensions. *Phys. Rev. Lett.* **101**, 194504.

XIA, H., SHATS, M. & FALKOVICH, G. 2009 Spectrally condensed turbulence in thin layers. *Phys. Fluids* **21**, 125101.